

Trustworthy predictive distributions for rare events via diagnostic transport maps

Elizabeth Cucuzzella¹, Rafael Izbicki² and Ann B. Lee¹

¹*Carnegie Mellon University Department of Statistics and Data Science, e-mail: ecucuzze@andrew.cmu.edu; annlee@andrew.cmu.edu*

²*Department of Statistics of the Federal University of São Carlos, e-mail: rafaelizbicki@gmail.com*

Abstract: Forecast systems in science and technology are increasingly moving beyond point prediction toward methods that produce full predictive distributions of future outcomes y , conditional on high-dimensional and complex sequences of inputs x . However, even when forecast systems provide a full predictive distribution, the result is rarely calibrated with respect to all x and y . The estimated density can be especially unreliable in low-frequency or out-of-distribution regimes, where accurate uncertainty quantification and a means for human experts to verify results are most needed to establish trust in models. In this paper, we take an initial predictive distribution as given and treat it as a useful but potentially misspecified base model. We then introduce *diagnostic transport maps*, covariate-dependent probability-to-probability maps that quantify how the base model’s probabilities should be adjusted to better match the true conditional distribution of calibration data. At deployment, these maps provide the user with real-time local diagnostics that reveal where the model fails and how it fails (including bias, dispersion, skewness, and tail errors), while also producing a recalibrated predictive distribution through a simple composition with the base model. We apply diagnostic transport maps to short-term tropical cyclone intensity forecasting and show that an easy-to-fit parametric version identifies evolutionary modes associated with local miscalibration and improves predictive performance for rare events, including 24-hour rapid intensity change, as compared to the operational forecasts of the National Hurricane Center.

1. Introduction

Machine learning research is steadily moving beyond simple point prediction towards methods that also quantify uncertainty. This shift reflects the fact that many real-world decisions require not only a single best guess, but also an understanding of how reliable that estimate is. In practice, uncertainty is often summarized through prediction intervals or selected quantiles, commonly trained using scoring rules such as the pinball loss [16, 12]. These summaries of uncertainties can be useful, but they provide only a partial view of a richer object: *the full conditional predictive distribution of future observations*. In particular, prediction intervals and single quantiles do not reveal whether the forecast captures the broader distributional structure correctly, including tail behavior, asymmetry, or multiple plausible modes. When decisions depend on these characteristics, the full predictive distribution—including information about how the distribution of future outcomes varies conditional on specific input sequences—must be reliable, and verifiable.

However, many probabilistic forecasting systems only obtain predictive distributions indirectly by multiple runs; off-the-shelf models are also rarely calibrated at a granular level.

A common strategy in both physics-based forecasting and AI-based generative modeling is to represent uncertainty through an ensemble of point forecasts and then convert that ensemble into a statistical distribution. In numerical weather prediction, for example, multiple runs with perturbed initial conditions produce a collection of plausible outcomes that is then post-processed into a predictive statistical distribution, often through a simple parametric approximation [32]. Similar strategies appear in AI systems, where repeated stochastic queries, sampling-based decoding, tokens or model ensembles are used to generate probabilistic forecasts [28, 38, 37]. These approaches are flexible, but require large amounts of train data, and can be especially unreliable in parts of the input space that are underrepresented in historical data. As a result, even when a forecast model outputs a full predictive distribution, it may still misrepresent uncertainty precisely where accurate uncertainty quantification matters most. Moreover, standard statistical and machine-learning objectives, including proper scoring rules [14], typically provide only global assessments of predictive performance—averaged over all possible inputs—and do not by themselves identify where in the input space the forecast is locally failing.

In this paper, we take an initial predictive distribution $\widehat{F}(\cdot | x)$ as given and treat it as a useful but potentially misspecified base model. Our goal is twofold:

- **(Local diagnostics)** We ask for which covariate values x and outcome levels y the base model $\widehat{F}(\cdot | x)$ is locally miscalibrated, and how those failures can be computed and visualized in a way that is interpretable to human experts. That is, we ask *where* the model can be trusted.
- **(Recalibration)** We then ask whether the base model can be reshaped, at deployment time, into a recalibrated distribution $\widetilde{F}(\cdot | x)$ that is closer to the true conditional distribution, especially with respect to conditional calibration, while preserving the structure already encoded in \widehat{F} . That is, rather than directly fitting target data from scratch, we ask *how* to transport the base model toward a target sample.

To address both questions, we introduce *diagnostic transport maps*: probability-to-probability maps that quantify, for each x , how the base model’s probabilities should be adjusted to better match the true distribution of the target, a.k.a “calibration” data (see Section 3.4 and Figure 2). These maps concentrate correction where calibration matters most, targeting the regions of the joint (x, y) -space in which the base model is least reliable (see Figure 1 for an example). This viewpoint is model-agnostic, computationally efficient at deployment even for complex high-dimensional data, and aimed directly at achieving the full predictive distribution rather than a single interval or quantile.

Our focus is motivated in part by rare events, where uncertainty quantification is most needed and standard training-based models are most likely to fail. In particular, models trained primarily on historical data often struggle in low-frequency or out-of-distribution regimes, where limited calibration data and distribution shift make both diagnosis and recalibration difficult. We show that diagnostic transport maps provide a practical way to address this problem, including in the tails of the predictive distribution. As a running application, we consider short-term tropical cyclone intensity forecasting, where accurate probabilistic guidance for rapid 24-hour intensity changes remains difficult for both physics-based and AI-based systems

[2], and where it is especially important for human experts to be able to relate forecasts from different guidance tools to observed physical processes and environmental conditions ahead of a rapid intensification. In that setting, our framework yields real-time deployable methods with easily digestible local diagnostics, and a mechanism to immediately produce predictive distributions that significantly improves upon the operational base model from the National Hurricane Center (NHC) given the observed sequence of inputs.

Our paper is organized as follows: In Section 2, we introduce rare events and tail events as two related but distinct notions of extreme behavior. In Section 3, we outline the basic set-up, introducing core ideas like local diagnostics and conditional recalibration. We also show that the diagnostic transport map corresponds to an optimal transport. In Section 4, we describe how to implement diagnostic transport maps in practice using both parametric and nonparametric models, which is then followed by an analysis of the theoretical properties of the two model choices in Section 5. Section 6 illustrates our methods on a synthetic example with a known predictive distribution. Section 7 finally showcases diagnostic transport maps on short-term TC intensity forecasting. We conclude with a discussion of our methodology and some future areas of work.

1.1. Relation to other work

PIT-based diagnostics. Classical diagnostics for predictive distributions often rely on the probability integral transform (PIT): if a predictive CDF $\widehat{F}(\cdot | x)$ is well calibrated, then $\widehat{F}(Y | X)$ should be uniformly distributed [16]. In practice, however, marginal PIT diagnostics only assess calibration on average and can hide substantial failures in specific parts of the covariate space. The local diagnostic framework of [36] addresses this problem by modeling the conditional distribution of the PIT given $X = x$. The framework in [11] further showed that these local PIT diagnostics can be used to reshape an initial conditional density estimate. The present paper builds on that line of work, but shifts the emphasis in two ways. First, the conditional PIT-CDF is treated explicitly as a probability-to-probability map that transports a base model toward the true conditional distribution represented by target data; this perspective is also reflected in Figure 2. Second, the focus is on parametric modeling of that map. This emphasis is motivated by the small-sample regimes that arise for rare and tail events: in precisely those regions of (x, y) -space where calibration matters most, calibration data are sparse, and a fully nonparametric estimate of the conditional PIT-CDF can become unstable or noisy. A parametric transport map imposes structure that stabilizes estimation, yields more reliable tail corrections, and makes recalibration feasible even when the relevant events are only weakly represented in the calibration sample.

Quantile-based methods and tail probabilities. Quantile regression and related procedures are used to estimate tail quantiles, prediction intervals, and threshold-specific risks [9, 13]. In particular, the quantile aggregation framework of [12] is close in spirit in that it allows the analyst to place greater weight on the quantile regions that matter for the problem at hand; see also the discussion of quantile- and threshold-weighted scoring rules in Appendix C. The main difference is the statistical target. Quantile methods focus on estimating selected

quantiles, or on combining quantile estimates across levels, whereas diagnostic transport maps recalibrate an entire conditional predictive distribution in one step. Once the transport map is estimated, all quantiles of the recalibrated predictive distribution are available simultaneously as a by-product. This removes the need to fit separate models across quantile levels, avoids quantile crossing by construction, and lets the user recover tail probabilities, prediction intervals, and quantiles from the same corrected predictive distribution.

Conformal prediction and predictive sets. Conformal methods are often used to obtain finite-sample valid prediction sets under exchangeability, typically in the sense of marginal coverage [34, 27]. More recent variants aim to improve adaptivity across the covariate space and approximate conditional validity [29, 8, 20, 21, 4]. There is also related work on conformal predictive distributions, including Mondrian conformal predictive distributions [3], which apply category-wise calibration across bins of the initial predictions, and recent flow-based conformal predictive distributions [19], which efficiently sample conformal boundaries via flows and then assemble the boundary samples into a single predictive distribution. Diagnostic transport maps are closer to this distributional line of research, but differ in that our methods learn a smooth, covariate-dependent map $\alpha \mapsto G(\alpha | x)$ that both recalibrates the initial predictive distribution and serves as an interpretable diagnostic: its shape reveals how the base model fails locally. Prediction sets at any desired level can then be read off from the recalibrated distribution, whereas prediction sets alone do not recover this local structure.

Scoring rules and distributional evaluation. Proper scoring rules such as the continuous ranked probability score (CRPS) are central tools for training and evaluating probabilistic forecasts [15, 12]. Weighted scoring rules are particularly useful when tail behavior or threshold events deserve extra emphasis. Our approach is complementary rather than an alternative to this literature: scoring rules provide global objectives for fitting and comparing predictive distributions, whereas the transport-map perspective adds a local, x -specific diagnostic and recalibration mechanism. In particular, it addresses a question that a global score does not answer directly: *how should a given predictive distribution be reshaped at the current input x ?*

2. Rare events and tail events

We consider two related but distinct notions of extreme behavior:

Tail events (given $X = x$). These are outcomes that lie in the far lower or upper tail of the predictive distribution for $Y | X = x$. For a tail level $\alpha < 0.5$, let $q_\alpha(x) := F^{-1}(\alpha | x)$ be the conditional quantile function. Then the lower and upper α -tail events are

$$\{Y \leq q_\alpha(x)\} \quad \text{and} \quad \{Y \geq q_{1-\alpha}(x)\}.$$

Tail events are thus defined relative to the conditional distribution at the current covariates x . Tail events are often rare events, but the two notions are not equivalent.

Rare events (in the joint set of covariates). Rare events are events that have small probability under the overall data-generating process, typically because they require an unusual combination of covariates and/or an extreme response. Formally, a rare event is a measurable set $A \subseteq \mathcal{X} \times \mathcal{Y}$ such that $\mathbb{P}((X, Y) \in A)$ is small. This includes, for example:

- “extreme Y given typical x ” (a tail event that occurs at commonly observed covariates),
- “typical Y but unusual x ” (rare covariate regimes),
- “extreme Y in an unusual x regime” (both rare and tail event).

Rare events are challenging to any training-based statistical or machine learning approach: even if a method is statistically sound, the fit can be poor in the parts of (x, y) -space where there are not enough calibration data.

3. The basics of diagnostic transport maps

3.1. Set-up and notation

We consider a supervised learning setting with covariates $X \in \mathcal{X} \subset \mathbb{R}^d$ and a continuous response $Y \in \mathcal{Y} \subset \mathbb{R}$. We denote the true conditional (predictive) CDF of Y given $X = x$ by $F(y | x) := \mathbb{P}(Y \leq y | X = x)$. To diagnose and reshape \widehat{F} we assume access to a calibration sample $\mathcal{T}_{\text{cal}} = \{(X_i, Y_i)\}_{i=1}^N$, which is independent of the data used to produce the base model \widehat{F} .

3.2. Local diagnostics based on PIT

Our approach analyzes the distribution of the probability integral transform (PIT) across the covariate space \mathcal{X} : Given a fixed initial predictive distribution $\widehat{F}(\cdot | x)$, we define a PIT variable for each observation (X, Y) ,

$$Z := \widehat{F}(Y | X).$$

That is, for each (X, Y) , we evaluate the CDF of the base model at the realized outcome Y .

For a fixed covariate value $x \in \mathcal{X}$, we then define the *conditional PIT-CDF* as

$$G(\alpha | x) := \mathbb{P}(Z \leq \alpha | X = x), \quad (1)$$

where $\alpha \in [0, 1]$. Intuitively, $G(\cdot | x)$ describes how the PIT values are distributed at covariate value x . The base model is perfectly calibrated at x if, and only if, $Z | X = x$ is Uniform $[0, 1]$, that is

$$G(\alpha | x) = \alpha \text{ for every } \alpha \in [0, 1].$$

It is the *dependence on x* that is interesting in regression and prediction problems, and that standard PIT and other popular diagnostics approaches do not model well.

3.3. Recalibrating the base model across the covariate space

Next we address the question of how to reshape the “base” density $\widehat{f}(\cdot | x)$ to the “target” density $f(\cdot | x)$ of the calibration sample. The key observation underlying our proposed approach is that the true predictive CDF $F(\cdot | x)$ can be written as a composition of the CDF of the known base model $\widehat{F}(\cdot | x)$ and the (in practice, unknown) true conditional PIT-CDF $G(\cdot | x)$. The following lemma formalizes this oracle representation:

Lemma 3.1. *Fix $x \in \mathcal{X}$ and assume that the initial predictive CDF $\widehat{F}(\cdot | x)$ is strictly increasing and continuous in y . For every $y \in \mathcal{Y}$,*

$$F(y | x) = \mathbb{P}(Y \leq y | X = x) = G(\widehat{F}(y | x) | x).$$

Lemma 3.1 shows that recalibrating the base CDF model $\widehat{F}(\cdot | x)$ is equivalent to estimating a family $\{G_x : x \in \mathcal{X}\}$ of *diagnostic transport maps*

$$G_X : \alpha \mapsto G(\alpha | x) \tag{2}$$

with $G_x(\alpha) := G(\alpha | x)$, which transforms the original probabilities into calibrated probabilities for every $\alpha \in [0, 1]$ and $x \in \mathcal{X}$.

By regression, we can obtain an estimate of the conditional PIT-CDF $G(\cdot | x)$ (Equation 1) and hence an estimate of the entire family of transport maps for $x \in \mathcal{X}$. We define the recalibrated predictive distribution as follows:

Definition 3.2 (Recalibrated predictive distribution). The recalibrated predictive CDF of Y given x is defined by

$$\widetilde{F}(y|x) := \widehat{G}_x \left(\widehat{F}(y|x) \right), \tag{3}$$

where \widehat{G}_x is an estimate of G_x .

Figure 1 summarizes the key idea and utility of diagnostic transport maps G_X . These maps (i) pinpoint the feature space regions in \mathcal{X} where the base model is a poor fit, (ii) directly convey the failure mode (bias, dispersion, skewness, tail weight, etc.) via PIT-CDF diagnostic plots (see Appendix A for interpretation), and (iii) offer a mechanism to recalibrate the predictive distribution. No other approach in the literature offers a general unified framework to local diagnostics and recalibration of PDs, which can be adapted to any type of data x and initial predictive distribution.

Finally, forecasters are often interested in the quality of estimating the probability of a binary event $\{Y \leq t\}$ at some pre-determined threshold $t \in \mathbb{R}$; for example, TC forecasters are interested in estimating the probability that a storm’s intensity is less than or equal to hurricane intensity (63 knots) at time $t + 24$ hours. Lemma 3.3 directly relates the error in (thresholded) probability forecasts to the error in the PIT-CDF estimates (or equivalently, the local diagnostic plots in Figure 1):

Corollary 3.3 (Error in probability forecasts). *Let $F(t | x) = \mathbb{P}(Y \leq t | x)$ with initial estimate $p = \widehat{F}(t | x)$. For every fixed $x \in \mathcal{X}$ and threshold $t \in \mathbb{R}$,*

$$\left| \widetilde{F}(t | x) - F(t | x) \right| = \left| \widehat{G}_x(p) - G_x(p) \right|$$

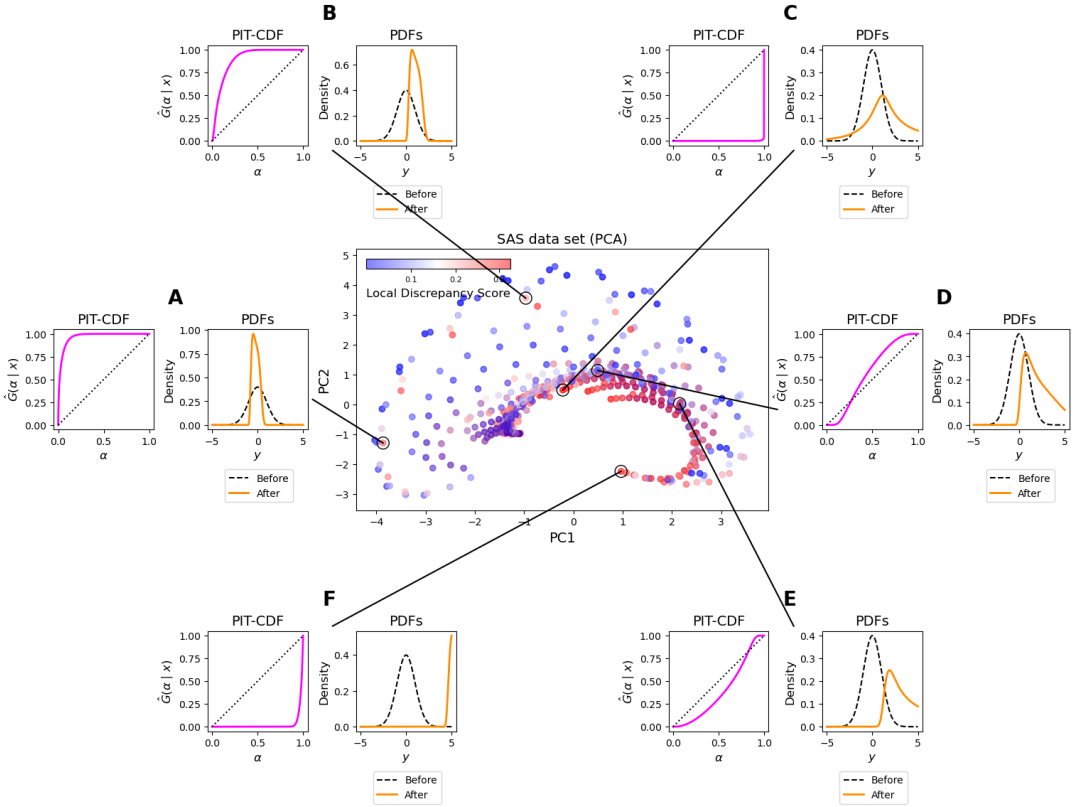


Fig 1. Synthetic example illustrating diagnostic transport maps. In this example, the true (unknown) predictive distribution $F(y|x)$ follows a *sinh-arcsinh* distribution with a shape that varies with x ; see Section 6 for details. From calibration data (pairs of (x, y) -variables), we estimate a diagnostic map that transports a Gaussian base model to a reshaped distribution that better approximates the predictive distribution for all x and y . The central image in the figure depicts the first two principal components (PCs) of the input space with the color of each test point encoding the estimated “local discrepancy score” (Equation 11); this score provides the scientist with guidance on how far the original base model is from the true predictive distribution for different x -values. The surrounding insets show some examples of how the scientist can then “zoom in” on specific locations to view the estimated PIT-CDF diagnostics (here nonparametric diagnostic transport map) that provide detailed information on the failure; each matching plot to the right shows the base and reshaped PDFs “before” and “after” applying the transport map. The PIT-CDFs of the outer bands of the “data manifold” in PC space signal a positive bias of the base model, whereas the the PIT-CDFs of the inner band signal a negative bias. Moving clockwise along the manifold, we see PIT-CDF diagnostics that signal over- to under-dispersion due to changing skewness and tail-weight of the true predictive CDF.

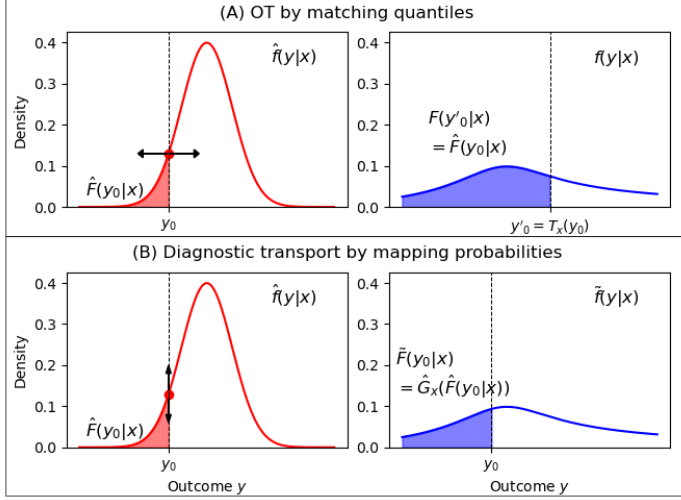


Fig 2. **Diagnostic maps as the solution to an optimal transport problem.** Top (A): A standard optimal transport (OT) map from $\widehat{F}(y | x)$ to $F(y | x)$ uses quantile matching for fixed x to match calibration data, where the OT map is given by $T_x(y_0) := F^{-1}(\widehat{F}(y_0 | x) | x)$. The OT map rearranges one PDF into another in outcome space, as indicated by the left-right double arrows. In practice, the true target distribution F is not known, and an OT map is also not designed to provide diagnostics of a base model. Bottom (B): A diagnostic transport constructs an estimate of the entire conditional distribution $F(y | x)$ by mapping probabilities, yielding the recalibrated distribution $\widetilde{F}(y_0 | x) = \widehat{G}_x(\widehat{F}(y_0 | x))$ (Definition 3.2). We achieve an estimate of the entire family of OT maps via $\widetilde{T}(y_0 | x) := \widehat{F}^{-1}(\widetilde{F}(y_0 | x) | x)$ for all $x \in \mathcal{X}$ and $y_0 \in \mathcal{Y}$ (Proposition 3.4) via a single regression. That is, the diagnostic map reshapes the original PDF in probability space, as indicated by the top-bottom double arrows, but the end result of matching quantiles or mapping probabilities is the same at every x .

3.4. The diagnostic transport map corresponds to an optimal transport

The optimal transport (OT), which rearranges a source distribution $\widehat{F}(y | x)$ into a target distribution $F(y | x)$ in outcome space for fixed x , is given by $T_x(y) = F^{-1}(\widehat{F}(y | x) | x)$ [30]. Diagnostic transport maps can be seen as an algorithmic solution to estimating the entire family of OT maps across a potentially high-dimensional feature space via a *single* regression, which maps probabilities to probabilities, and directly targets local calibration.

Proposition 3.4 (OT map as a composition involving G). *Fix $x \in \mathcal{X}$ and assume that $F(\cdot | x)$, $\widehat{F}(\cdot | x)$, and $G(\cdot | x)$ are continuous and strictly increasing. Then, for any $y \in \mathcal{Y}$,*

$$T_x(y) = F^{-1}(\widehat{F}(y | x) | x) = \widehat{F}^{-1}\left(G^{-1}(\widehat{F}(y | x) | x) \mid x\right).$$

Figure 2 illustrates the parallel views of diagnostic transport maps and optimal transport. For further details and a proof of Proposition 3.4, see Appendix G.

4. Diagnostic transport maps in practice

The original calibration algorithm by [11] estimates $G(\cdot | x)$ nonparametrically using a monotonic neural network that regresses the binary event $\{\widehat{F}(Y | X) \leq \alpha\}$ on (α, X) . While a fully nonparametric approach is flexible and asymptotically consistent, it can produce noisy

or unstable predictive distributions when the calibration sample size N is moderate or small; this is especially a problem for rare events which exist in regions of (x, y) that are poorly covered by the calibration data. To better handle rare event regimes, we propose a *parametric* version of diagnostic transport maps in Section 4.1. In data-rich settings and for complex base models, we recommend a nonparametric version (Section 4.2).

4.1. Parametric transport map via local PIT parameterization

In many scientific applications, calibration data are often limited in size, making it difficult to solve for $\widehat{G}(\cdot | x)$ nonparametrically. Therefore, instead of learning an arbitrary function $(\alpha, x) \mapsto G(\alpha | x)$, we posit that for each $x \in \mathcal{X}$ the conditional distribution of $Z | X = x$ belongs to a parametric family on $[0, 1]$, indexed by a *local parameter* $\theta(x) \in \Theta \subset \mathbb{R}^p$:

$$G(\alpha | x) \approx G_{\theta(x)}(\alpha)$$

Here, G_θ denotes a CDF on $[0, 1]$ for each $\theta \in \Theta$ (e.g. a Beta, Kumaraswamy, or other flexible distribution on $[0, 1]$ that has the Uniform as a special case.) The map $x \mapsto \theta(x)$ is learned from the calibration data and can be represented by a shallow neural network, a generalized linear model, or any other smooth regression mechanism.¹

Given the calibration sample $\mathcal{T}_{\text{cal}} = \{(X_i, Y_i)\}_{i=1}^N$, we form the PIT values

$$Z_i := \widehat{F}(Y_i | X_i), \quad i = 1, \dots, N.$$

We then fit the function $x \mapsto \theta(x)$ by (for example) maximizing the conditional likelihood of Z_i under the parametric PIT model $Z_i | X_i = x \sim G_{\theta(x)}$, or more generally by minimizing an empirical loss

$$\frac{1}{N} \sum_{i=1}^N L(Z_i, X_i; \theta(\cdot)),$$

where L is a proper scoring rule associated with the family $\{G_\theta\}$. The result is an estimated parameter function $\widehat{\theta}(x)$ and an estimated PIT-CDF

$$\widehat{G}(\alpha | x) := G_{\widehat{\theta}(x)}(\alpha).$$

The recalibrated predictive CDF for $Y | X = x$ is then obtained by composition:

$$\widetilde{F}(y | x) := \widehat{G}(\widehat{F}(y | x) | x) = G_{\widehat{\theta}(x)}(\widehat{F}(y | x)). \quad (4)$$

When both the original predictive distribution and the PIT model admit densities, the calibrated *density* can also be obtained in closed form. Let $\widehat{f}(y | x) := \partial_y \widehat{F}(y | x)$ denote the initial conditional density of $Y | X = x$, and let $g_\theta(\alpha) := \partial_\alpha G_\theta(\alpha)$ denote the density of Z under the PIT model. Differentiating the composition $\widetilde{F}(y | x) = G_{\widehat{\theta}(x)}(\widehat{F}(y | x))$ with respect to y yields, by the chain rule,

$$\widetilde{f}(y | x) := \partial_y \widetilde{F}(y | x) = g_{\widehat{\theta}(x)}(\widehat{F}(y | x)) \widehat{f}(y | x). \quad (5)$$

That is, the parametric transport map correction rescales the initial density estimate by the PIT density evaluated at the base model CDF value.

¹Alternatively, one could also use a *semiparametric* approach, where the PIT family is parametric but the map $x \mapsto \theta(x)$ is modeled nonparametrically.

4.2. Nonparametric transport map via deep monotonic neural networks

In data-rich settings, we recommend a nonparametric approach that can learn arbitrary functions $(\alpha, x) \mapsto G(\alpha | x)$. We refer to [11] for a statistical procedure that leverages deep monotonic neural networks to estimate the conditional PIT-CDF, where the model architecture depends on the calibration data and its size N .

5. Theoretical properties of parametric diagnostic transport maps

Next we formalize the parametric transport map procedure and derive error bounds that separate approximation (model misspecification) and estimation effects. The details are in Appendix H. We then contrast these bounds with those for a fully nonparametric PIT estimator and discuss the resulting trade-offs.

5.1. Reparameterization trick and the best-in-family solution

In this section, we describe the family of distributions induced by the parametric map $(\alpha, x) \mapsto G_{\theta(x)}(\alpha)$ as $\{G_{\beta}(\cdot | x) : \beta \in \mathcal{B} \subset \mathbb{R}^q\}$, where β are the internal parameters of, for example, a neural network that encodes the relationship between x and θ , so that $\theta(x) := \theta(x; \beta)$. Given the calibration data, we estimate β by minimizing a suitable empirical loss (e.g. negative log-likelihood or another proper scoring rule) yielding

$$\hat{\beta} = \arg \min_{\beta \in \mathcal{B}} \frac{1}{N} \sum_{i=1}^N L(Z_i, X_i; \beta),$$

where $L(\cdot, \cdot; \beta)$ is a pointwise loss function that compares the PIT value Z_i to the model $G_{\beta}(\cdot | X_i)$.

We then define the fitted PIT-CDF,

$$\widehat{G}(\alpha | x) := G_{\hat{\beta}}(\alpha | x),$$

and the corresponding calibrated predictive CDF, $\widetilde{F}(y | x) := \widehat{G}(\widehat{F}(y | x) | x) = G_{\hat{\beta}}(\widehat{F}(y | x) | x)$.

We define the *population* risk as

$$R(\beta) := \mathbb{E}[L(Z, X; \beta)],$$

and we define a best-in-family parameter:

Definition 5.1 (Best-in-family PIT parameter). A parameter β^* is called a best-in-family (or oracle) PIT parameter if

$$\beta^* = \arg \min_{\beta \in \mathcal{B}} R(\beta).$$

We denote the corresponding PIT-CDF by $G^*(\cdot | x) := G_{\beta^*}(\cdot | x)$.

That is, $G^*(\cdot | x)$ is the transport map within the chosen parametric family that best approximates the true map $G(\cdot | x)$ on average with respect to the joint distribution of (X, Z) .

5.2. Decomposition of the pointwise error in the reshaped predictive distribution

For fixed $x \in \mathcal{X}$, we consider the integrated squared error

$$\mathcal{E}(x) := \int_{\mathcal{Y}} (F(y | x) - \tilde{F}(y | x))^2 w(dy), \quad (6)$$

for an arbitrary weight measure w on \mathcal{Y} .

We then relate the error in the reshaped predictive distribution \tilde{F} at a point (x, y) to the discrepancy between the true transport map G and its parametric approximation at the probability $p := \tilde{F}(y | x) \in [0, 1]$.

Proposition 5.2 (Error in reshaped PD). *Fix $x \in \mathcal{X}$ and $y \in \mathcal{Y}$, and let $p := \tilde{F}(y | x)$. Then*

$$|F(y | x) - \tilde{F}(y | x)| \leq \underbrace{|G(p | x) - G^*(p | x)|}_{\text{PIT model misspecification}} + \underbrace{|G^*(p | x) - G_{\hat{\beta}}(p | x)|}_{\text{estimation error}}.$$

The first term captures the irreducible bias due to the limited complexity of the parametric family $\{G_{\beta}\}$ (“PIT model misspecification”). The second term reflects the discrepancy between the oracle parameter β^* and its empirical estimate $\hat{\beta}$ due to finite calibration data (“estimation error”).

5.3. Parametric versus nonparametric diagnostic transport maps

In Appendix H we derive parametric rates of the integrated error under the assumption that the PIT-CDF is locally Lipschitz in the parameter vector β . Suppose the parametric PIT family is reasonably well specified in the sense that

$$\sup_{x,y} |G(p_y | x) - G^*(p_y | x)| \leq \delta,$$

for some small $\delta > 0$ where $p_y := \tilde{F}(y | x)$. Then Theorem H.2 implies

$$\mathbb{E}[\mathcal{E}(x)] \leq 2\delta^2 + \frac{2\tilde{C}(x)}{N}. \quad (7)$$

By Markov’s inequality, this implies the probabilistic bound

$$\mathcal{E}(x) = 2\delta^2 + O_{\mathbb{P}}(N^{-1}). \quad (8)$$

On the other hand, the integrated nonparametric error typically satisfies

$$\mathcal{E}^{\text{np}}(x) = O_{\mathbb{P}}(N^{-2\kappa}), \quad (9)$$

where $\kappa = s/(2s + d)$, with no explicit model-bias term: the nonparametric estimator can, in principle, approximate G arbitrarily well as $N \rightarrow \infty$ (Appendix H.2).

Comparing (8) and (9), we obtain the following:

- *Parametric transport maps* attain a fast N^{-1} decay of the integrated estimation error, but suffer from a non-vanishing bias term δ^2 whenever the PIT family is misspecified.

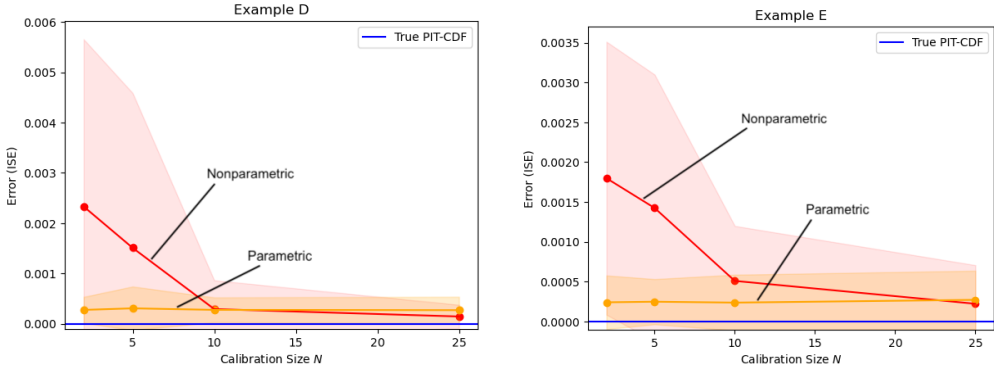


Fig 3. **Convergence rates of parametric versus nonparametric diagnostic transport maps.** The left and right panels show the integrated squared error (ISE; Equation 6) as a function of the calibration size N for test points (or “Examples”) D and E in Figure 1. The curves and shaded areas represent the average ISE plus/minus two standard deviations for $B = 25$ simulated calibration sets. Although parametric transport maps have non-vanishing model bias, their ISE decays much faster than nonparametric transport maps, effectively leading to more accurate estimates of the predictive distributions in the challenging small- N regime, which is relevant for rare events.

- *Nonparametric transport maps* have no such model-bias term, but its estimation error decays at the slower rate $N^{-2\kappa}$, which deteriorates as the covariate dimension d increases or the smoothness index s decreases.

As a consequence, when the parametric PIT model is only mildly misspecified (small δ) and the covariate dimension d is moderate or large, parametric maps are expected to yield smaller integrated calibration error in the practically relevant “small- N ” regime. Nonparametric maps become advantageous once a very large calibration sample is available, as their approximation error can vanish while the parametric bias term δ^2 remains.

Next we illustrate these trade-offs for a synthetic example with a family of prediction distributions that has been suggested in the environmental science literature [1] to model tropical cyclone intensity distributions.

6. Synthetic example

Set-up. For our synthetic example, we choose a predictive distribution from the four-parameter sinh-arcsinh (SAS) distribution [23]

$$S_{\mu, \sigma, \epsilon, \delta}(t) = \Phi \left(\sinh \left(\delta \operatorname{arcsinh} \left(\frac{t - \mu}{\sigma} \right) - \epsilon \right) \right),$$

where Φ denotes the CDF of a standard normal random variable. The parameters $\mu \in \mathbb{R}$, $\sigma \in \mathbb{R}^+$, $\epsilon \in \mathbb{R}$, $\delta \in \mathbb{R}^+$, respectively, account for location, scale, skewness, and tail-weight, with the special case $\mu = \epsilon = 0$ and $\sigma = \delta = 1$ corresponding to the standard normal. To create a predictive distribution with different shapes, we assume a four-dimensional predictor $\mathbf{x} = (x_1, x_2, x_3, x_4)$ and a true (but assumed to be unknown) predictive CDF $F(y|\mathbf{x}) = S_{x_1, x_2, x_3, x_4}(y)$, where each SAS shape parameter varies with one predictor

dimension. Our base model is the standard normal, $\widehat{F}(y | \mathbf{x}) = \Phi(y)$ for all \mathbf{x} . We have access to calibration data $\mathcal{T}_{\text{cal}} = \{(\mathbf{x}_1, y_1), \dots, (\mathbf{x}_N, y_N)\}$, where the predictors \mathbf{x}_i , for $i=1, 2, \dots, N$, are drawn uniformly from the set $S = [-2, 2] \times (0, 2] \times [-2, 2] \times (0, 2]$, and the response variables y_i are drawn from $F(y_i | \mathbf{x}_i)$.

Diagnostic transport maps. We learn the diagnostic transport maps (Equation 2) from the calibration set \mathcal{T}_{cal} by estimating the conditional PIT-CDF $G(\alpha | \mathbf{x})$ in Equation 1 either parametrically or non-parametrically. In the *parametric* case, we approximate the PIT-CDF at fixed \mathbf{x} with a two-parameter Kumaraswamy distribution [22, 25]

$$G_{a,b}(\alpha) = 1 - (1 - \alpha^a)^b,$$

which is a beta-type distribution (it is defined on $[0, 1]$ and includes the uniform distribution) with closed-form expressions for its CDF, PDF, and quantile function. We learn the maximum likelihood estimates of a and b as a function of \mathbf{x} with a three-layer (max 64 units/layer) neural network with ReLU activation that minimizes the negative log-likelihood. In the *nonparametric* case, we fit $G(\alpha | \mathbf{x})$ with a monotonic neural network [35] that scaled with calibration size.

Results. Figure 1 shows examples of local PIT-CDFs learned via diagnostic transport maps, together with the corresponding predictive PDFs before and after a recalibration via Equation 3. Once we have learned the transformation, the evaluation of the transport map at different \mathbf{x} -values is instantaneous. The data analyst can easily produce similar visualizations to assess the base model and reshape predictive PDFs to match calibration data.

Because this is a synthetic example, we can derive the true conditional PIT-CDF, $G(\alpha | \mathbf{x}) = F(\Phi^{-1}(\alpha) | \mathbf{x})$ (see Appendix I for derivation) and then compute the integrated squared error (ISE) of the estimated parametric and nonparametric transport maps according to Equation 14. We are interested in the convergence rate of the parametric and nonparametric diagnostic maps. Using Monte Carlo simulation, we generate $B = 25$ \mathcal{T}_{cal} -sets at calibration sample sizes $N = 2, \dots, 200$. Training results in $N \times B$ parametric and $N \times B$ nonparametric maps. We evaluate the ISE for each map on a fixed grid of \mathbf{x} -values, and report the mean and standard deviation of the ISE for B Monte Carlo samples. Figure 3 shows that the parametric diagnostic map (blue) outperforms the nonparametric map (red) for small N . As the calibration sample size N increases, the “Nonparametric PIT-CDF” approaches the “True PIT-CDF” (orange), which by construction has $ISE = 0$, whereas the parametric map approaches the best solution in the Kumaraswamy distribution, which has a small, but non-zero, ISE.

7. Key application: Improving predictive distributions of short-range TC intensity

7.1. Data and initial distribution of forecast intensity errors

Human forecasters at the National Hurricane Center (NHC) issue short-range (e.g. 24-hour) forecasts of tropical cyclone (TC) intensities using multiple statistical, AI, and physics-based models. The NHC’s Official Forecast (OFCL) typically has higher skill than any single model

because human experts weight various models based on environmental conditions. Nevertheless, the task of digesting multiple inputs in real-time is challenging for human forecasters. In addition, both physics and AI models can struggle with predicting potentially devastating “rapid intensification” (RI) events, which are defined as phenomena where a storm’s maximum sustained winds increase by at least 30 knots (35 mph) in a single day. Hence, an improvement in real-time 24-hour guidance with diagnostics that are easily interpretable to human forecasters can have a large positive impact on emergency response and disaster preparedness.

The NHC keeps a historical database of their official forecasts and forecast errors over the years [6]. The NHC “forecast intensity error” is defined as the difference between the official point forecast and the best track intensity at the forecast verifying time. Statistical uncertainty is typically taken as an average of these errors over several years of record. Following [32], we represent NHC intensity errors by a Gaussian distribution $N(\epsilon_{t+24}, \sigma^2)$, where the mean ϵ_{t+24} is the NHC forecast intensity error at $t+24$ hours, and the standard deviation σ is a ten-year average of NHC forecast intensity errors. We refer to this distribution as the NHC base error model.

Our goal is to assess and improve upon the base model using Statistical Hurricane Intensity Prediction Scheme (SHIPS; [10]) values. SHIPS is a statistical-dynamical model used by the NHC to forecast TC intensity changes at 12 to 72 hours with predictors that represent environmental values, including humidity, wind shear, and distance to land. Our transport maps use a subset of 13 SHIPS predictors and the intensities at times $t - 12$, $t - 6$, and t hours (14 total predictors); see Appendix J for details. We denote the entire 12-hour input sequence of 3×14 values by $\mathbf{S}_{\leq t}$ or just \mathbf{S} , and the density of residual errors at $t + 24$ hours by $f(\epsilon_{t+24} | \mathbf{S}_{\leq t})$ or just $f(\epsilon | \mathbf{S})$.

To learn the diagnostic transport maps, we use storms in the Atlantic basin from 2000-2015. We then evaluate the results on storms from 2016-2022. Table 1 lists available data (number of 36-hour sequences and number of unique TCs) for calibration and testing. Note that both RI and rapid weakening (RW) events with intensity change of more than 30 knots in 24 hours are rare events. Category 3-5 storm (hurricanes achieving a wind speed with more than 95 knots) are both rare events and tail events.

7.2. Results

Using the calibration data, we learn parametric and nonparametric diagnostic transport maps. The parametric map is fit using a three-layer convolutional neural network that feeds into a five-layer fully connected neural network (max 64 units/layer) with ReLU activation. We minimize the negative log-likelihood of the Kumaraswamy distribution to approximate the maximum likelihood estimators for a, b . The nonparametric map is a three-layer convolutional neural network feeding into a five-layer monotonic neural network that minimizes the Brier score with the number of units per layer varying based on calibration size N .

	# Sequences	# Unique TCs
(i) Calibration (2000-2015)		
Total	2395	171
RI	204	59
RW	60	25
TS	1159	167
Categories 1-2	519	90
Categories 3-5	271	36
(ii) Testing (2016-2022)		
Total	1274	95
RI	120	28
RW	30	13
TS	664	91
Categories 1-2	221	44
Categories 3-5	161	21

Table 1

Calibration and test data in TC application. (i) We train the diagnostic transport maps on 12-hour sequences of SHIPS predictors for Atlantic storms from 2000-2015. (ii) We assess the performance of $t+24$ hour intensity error distributions on storms from 2016-2022. The table lists the number of available sequences and the number of unique TCs. Hurricane categories follow the Saffir-Simpson scale with division into tropical storm (TS) and categories 1-5. Rapid intensification (RI) and rapid weakening (RW) events are storms that change by more than 30 knots within 24 hours.

7.3. Diagnostic insights

The initial predictive distribution might capture some TC evolutionary modes better than others. Our methodology provides insights that can be connected back to the underlying physical mechanisms. Figure 4 shows example diagnostics for a parametric diagnostic transport map. Figure 5 illustrates how a forecaster can deploy diagnostic transport maps in real time and assess whether the recommended corrections are consistent with physical processes and how the storm is evolving in time. Diagnostic transport maps improve the most upon NHC error distributions for intense storms (example of tail events) and rapid intensity change events (example of rare events). For example, the diagnostic plot in Figure 4 identifies Point B as an input sequence with an unreliable initial predictive distribution. A closer look (see Figure 5) shows that Point B corresponds to a 12-hour sequence of Hurricane Irma (2017) when the storm was a sustained Category 5 hurricane before making landfall. Figure 5 shows visuals for the corresponding evolutionary mode. In Appendix K.2 we show similar diagnostics and visuals for a poorly calibrated distribution that corresponds to a storm that is undergoing a rapid weakening event.

7.4. Improved prediction and uncertainty quantification

Next we examine whether parametric and nonparametric diagnostic transport maps improve upon the NHC official forecasts. An analysis shows that reshaping the initial error distributions with SHIPS calibration data results in improved performance across a variety of metrics and subdivisions of the test data. The top half of Table 2 lists the continuous ranked probability

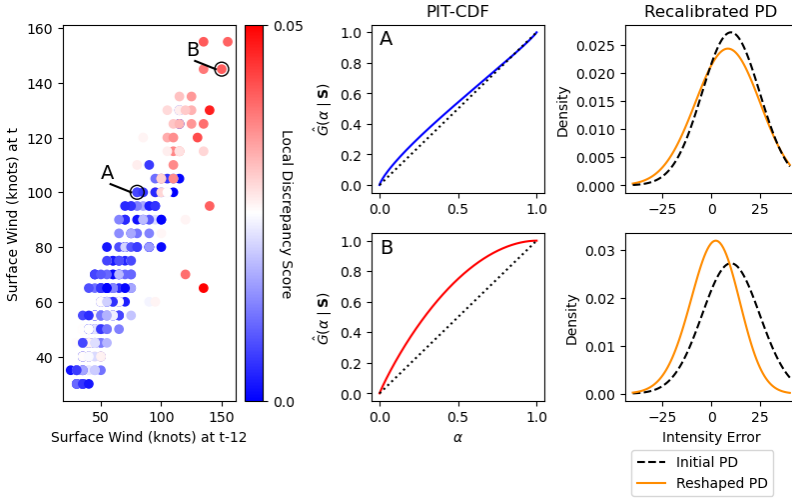


Fig 4. Diagnostic insights for TC application. Left: Each point in the graph represents a particular 12-hour input sequence $\mathbf{S}_{\leq t} = \{\mathbf{x}_{t-12}, \mathbf{x}_{t-6}, \mathbf{x}_t\}$, where each \mathbf{x} corresponds to SHIPS predictors and TC intensity at a particular instance of the storm's evolution. With a parametric diagnostic transport map, we can quickly compute a local discrepancy score (LDS) that assesses how well the initial error distribution of $t + 24$ h intensities matches the test data for that particular input sequence. **Point A** represents a storm sequence with low LDS (good fit). **Point B** represents a storm sequence that has a high LDS (poor fit). For simplicity, we are only displaying two SHIPS predictors here: the surface wind at times $t-12$ and $t-6$ hours. Center: Diagnostic plots for test points A and B. Note that Panel B has a shape that indicates that the base model of $+24$ -hour errors is positively biased; that is, the predictive distribution of TC intensities at $t+24$ hours is shifted upwards relative to the true TC intensity distribution. Right: Recalibrated PDFs (orange) of $+24$ -hour intensity errors after applying the estimated transport maps to the base models.

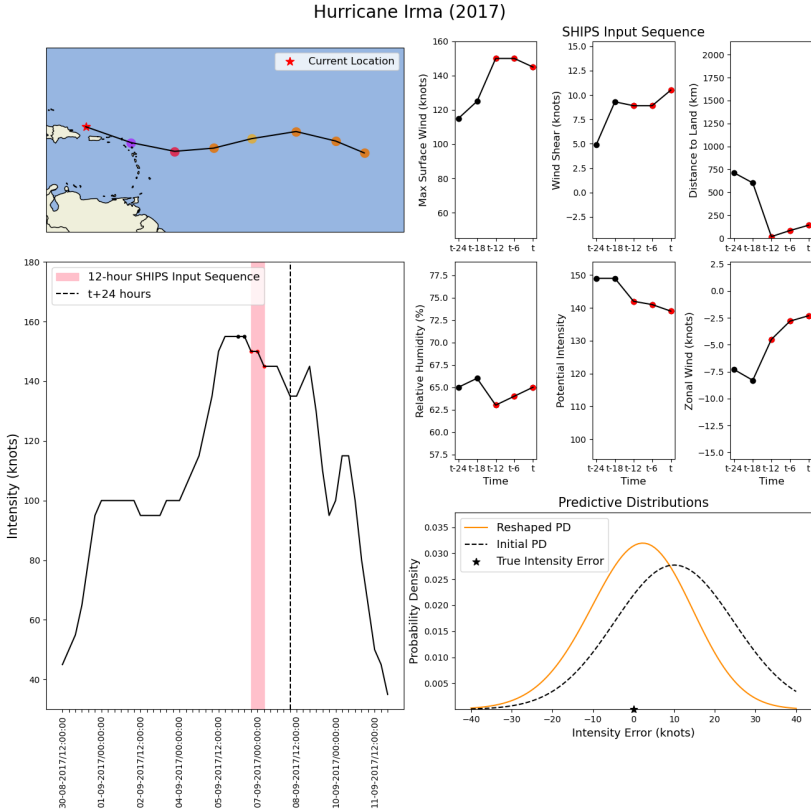


Fig 5. Example dashboard for TC scientists and forecasters. Diagnostic transport maps provide the user with local diagnostics and a mechanism for reshaping the base model in real time; no additional training is needed at deployment. Hence, a human expert can directly connect model output to physical processes and check whether the correction makes sense. Example B in Figure 4 corresponds to a specific evolutionary mode of Hurricane Irma (2017). This figure shows an example dashboard that can facilitate model verification; see [here](#) for a video. Top left: Track of Hurricane Irma (2017) with the intensity of the storm encoded by NHC’s color classification scheme from past track maps [7] at the synoptic times at 6-hour resolution. “Current location” corresponds to time t . Top right: Six SHIPS predictors shown from $t - 24$ to t . The red dots mark the values that are included in the 12-hour input sequence $\mathbf{S}_{\leq t}$. Bottom left: TC intensity as a function of time. The red band marks the time interval between $t - 12h$, to t . The vertical dashed line marks the time $t + 24h$ where we make our forecast. Bottom right: The error distribution $\tilde{f}(\epsilon_{t+24h} | \mathbf{S}_{\leq t})$ from NHC official forecasts (black dashed) and the reshaped error distribution $\tilde{f}(\epsilon_{t+24h} | \mathbf{S}_{\leq t})$ after applying parametric transport maps (solid orange). Here the recalibration shifts the mean of the base density toward 0 knots (the true intensity error), while also decreasing the variance resulting in a tighter prediction interval than for the base model.

CRPS			
Category	NHC Operational forecast	Nonparametric map	Parametric map
Overall	6.4	6.6 (+3.4%)	6.3 (-1.6%)
TS	5.5	5.5 (-1.3%)	5.4 (-2.2%)
Categories 1&2	7.4	8.0 (+7.7%)	7.4 (-1.1%)
Categories 3-5	7.5	7.7 (+2.1%)	7.5 (-0.5%)
RI	9.2	10.0 (+8.1%)	8.4 (-9.0%)
RW	7.9	6.0 (-23.9%)	5.9 (-25.7%)

RMSE			
Category	NHC Operational forecast	Nonparametric map	Parametric map
Overall	12.2	12.0 (-2.0%)	10.6 (-13.4%)
TS	10.0	9.8 (-1.4%)	9.1 (-9.1%)
Categories 1&2	14.3	14.2 (0.7%)	12.2 (-14.9%)
Categories 3-5	14.9	13.5 (-9.2%)	12.0 (-19.5%)
RI	18.0	16.7 (-7.4%)	14.5 (-19.6%)
RW	14.1	10.6 (-24.9%)	10.5 (-25.4%)

Table 2

Predictive performance of NHC operational model before and after recalibration. *The CRPS (scaled by a multiplicative factor of 100) (top) and the RMSE (bottom) of the TC intensity error distribution from the original base model (“NHC operational forecasts”), and after a recalibration with diagnostic transport maps (“Nonparametric map” and “Parametric map”) with the numbers in parenthesis denoting percentage improvement over the NHC operational forecast. The best performance in each row is marked in blue. The results show that the parametric approach improves the NHC error distribution in both CRPS and RMSE across the board, whereas the nonparametric approach improves for specific extreme events such as rapid weakenings.*

score (CRPS; Definition B.1), a measure of how well a full predictive distribution matches a realized outcome. The bottom half of the table lists the root mean square error (RMSE), a measure of the predictive accuracy of a point forecast derived from the error distribution. Here we compute the RMSE of the expected value of the estimated error distribution in knots relative to the true error, where the latter is 0 by construction.

The table shows that parametric diagnostic maps improve upon the NHC forecasts in both CRPS and RMSE, when the values are averaged across the entire test set (“Overall”) as well as when they are computed for storm subdivisions based on hurricane strengths or intensity change. The nonparametric maps are less successful but still decrease the RMSE across TC categories and the CRPS for RW events. The difference in performance between parametric and nonparametric approaches is consistent with previous analysis (Section 5 and Figure 3) that showed that the parametric maps lead to more accurate predictive distributions for limited calibration data. For the TC application, the most notable improvement in NHC results occur for parametric transport maps and rare events — more specifically, storms that undergo rapid intensity changes (RI and RW).

8. Discussion

In this paper, we show how diagnostic transport maps can identify input patterns or evolutionary modes associated with poor calibration of predictive distributions, and how these maps then can morph the initial model toward locally calibrated distributions. We demonstrate the effectiveness of a parametric version for settings where calibration data are limited and

accurate modeling of rare events is consequential. For tropical cyclone intensity forecasting, parametric diagnostic transport maps significantly improve operational NHC error distributions both on average and across a spectrum of extreme events. Although our framework was originally motivated by severe weather forecasting, the proposed framework can be used in any application where scientists and forecasters need easy-to-use tools to assess and recalibrate black-box forecasting models with respect to target data of interest. Parametric maps are most useful in small-sample settings, whereas nonparametric or semiparametric maps become more attractive when larger calibration samples are available, allowing greater flexibility in reshaping the base model. Future work involves extending diagnostic transport maps to multivariate response variables and spatio-temporal processes.

9. Acknowledgments

The authors would like to thank Dr Kimberly Wood from the University of Arizona Department of Hydrology and Atmospheric Sciences and Dr Tria McNeely at Microsoft for their helpful feedback and guidance on the TC application. Part of this work was funded by NSF DMS-2053804. RI is grateful for the financial support of CNPq (422705/2021-7, 305065/2023-8 and 403458/2025-0) and FAPESP (grant 2023/07068-1).

References

- [1] Elizabeth A. Barnes, Randal J. Barnes, and Mark DeMaria. Sinh-arcsinh-normal distributions to add uncertainty to neural network regression tasks: Application to tropical cyclone intensity forecasting. *Environmental Data Science*, 2, 2023.
- [2] Xinyuan Bi, Jingping Liu, and Yihong Duan. Review of artificial intelligence application in typhoon forecasting. *Tropical Cyclone Research and Review*, 14, 2025.
- [3] Henrik Boström, Ulf Johansson, and Tuwe Lofström. Mondrian conformal predictive distributions. In *Conformal and Probabilistic Prediction and Applications*, volume 152 of *Proceedings of Machine Learning Research*, pages 1–15. PMLR, 2021.
- [4] Luben M. C. Cabezas, Mateus P. Otto, Rafael Izbicki, and Rafael B. Stern. Regression trees for fast and adaptive prediction intervals. *Information Sciences*, 686:121369, 2025.
- [5] National Hurricane Center. Ships predictor files, 2023. URL https://rammb-data.cira.colostate.edu/ships/data/ships_predictor_file.pdf.
- [6] National Hurricane Center. National hurricane center forecast verification, 2025. URL <https://www.nhc.noaa.gov/verification/verify7.shtml>.
- [7] National Hurricane Center. Nhc data archive, 2025. URL https://www.nhc.noaa.gov/data/#tracks_all.
- [8] Victor Chernozhukov, Kaspar Wüthrich, and Yinchu Zhu. Distributional conformal prediction. *Proceedings of the National Academy of Sciences*, 118(48):e2107794118, 2021.
- [9] Youngseog Chung, Willie Neiswanger, Ian Char, and Jeff Schneider. Beyond pinball loss: Quantile methods for calibrated uncertainty quantification. *Advances in Neural Information Processing Systems*, 34:10971–10984, 2021.
- [10] Mark DeMaria and John Kaplan. A statistical hurricane intensity prediction scheme (ships) for the atlantic basin. *Weather and Forecasting*, 9, 1994.
- [11] Biprateep Dey, David Zhao, Brett Andrews, Jeffrey Newman, Rafael Izbicki, and Ann B. Lee. Towards instance-wise calibration: local amortized diagnostics and reshaping of conditional densities (ladar). *Machine Learning: Science and Technology*, 6(4), 2025.
- [12] Rasool Fakoor, Taesup Ki, Jonas Mueller, Alexander J. Smola, and Ryan J. Tibshirani. Flexible model aggregation for quantile regression. *Journal of Machine Learning Research*, 24(162), 2023.
- [13] Shai Feldman, Stephen Bates, and Yaniv Romano. Improving conditional coverage via orthogonal quantile regression. *Advances in neural information processing systems*, 34:2060–2071, 2021.
- [14] Tilmann Gneiting and Adrian E. Raftery. Strictly proper scoring rules, prediction, and estimation. *Journal of the American Statistical Association*, 2007.
- [15] Tilmann Gneiting and Roopesh Ranjan. Comparing density forecasts using threshold- and quantile-weighted scoring rules. *Journal of Business and Economic Statistics*, 9, 2011.
- [16] Tilmann Gneiting, Fadoua Balabdaoui, and Adrian E. Raftery. Probabilistic forecasts, calibration, and sharpness. *Journal of the Royal Statistical Society Series B: Statistical Methodology*, 69, 2007.

- [17] Peter Hall, Rodney C. L. Wolff, and Qiwei Yao. Methods for estimating a conditional distribution function. *Journal of the American Statistical Association*, 94(445):154–163, 1999.
- [18] Bruce E. Hansen. Nonparametric estimation of smooth conditional distributions. Working paper, University of Wisconsin, 2004.
- [19] Trevor Harris. Flow-based conformal predictive distributions. 2026.
- [20] Rafael Izbicki, Gilson Shimizu, and Rafael B. Stern. Flexible distribution-free conditional predictive bands using density estimators. In Silvia Chiappa and Roberto Calandra, editors, *Proceedings of the Twenty Third International Conference on Artificial Intelligence and Statistics*, volume 108 of *Proceedings of Machine Learning Research*, pages 3068–3077. PMLR, 2020.
- [21] Rafael Izbicki, Gilson Shimizu, and Rafael B. Stern. Cd-split and hpd-split: Efficient conformal regions in high dimensions. *Journal of Machine Learning Research*, 23(87): 1–32, 2022.
- [22] M.C. Jones. Kumaraswamy’s distribution: A beta-type distribution with some tractability advantages. *Statistical Methodology*, 6, 2009.
- [23] M.C. Jones and Arthur Pewsey. Sinh-arcsinh distributions. *Biometrika*, 96(4), 2009.
- [24] Soheil Kolouri, Se Rim Park, Matthew Thorpe, Dejan Slepcev, and Gustavo K Rohde. Optimal mass transport: Signal processing and machine-learning applications. *IEEE signal processing magazine*, 34(4):43–59, 2017.
- [25] P. Kumaraswamy. A generalized probability density function for double-bounded random processes. *Journal of Hydrology*, 46, 1980.
- [26] F. Laio and S. Tamea. Verification tools for probabilistic forecasts of continuous hydrological variables. *Earth and System Sciences*, 11, 2007.
- [27] Jing Lei, Max G’Sell, Alessandro Rinaldo, Ryan J. Tibshirani, and Larry Wasserman. Distribution-free predictive inference for regression. *Journal of the American Statistical Association*, 113(523):1094–1111, 2018.
- [28] Pengfei Liu, Weizhe Yuan, Jinlan Fu, Zhengbao Jiang, Hiroaki Hiyashi, and Graham Neubig. Pre-train, prompt, and predict: A systematic survey of prompting methods in natural language processing. *ACM Computing Surveys*, 55, 2023.
- [29] Yaniv Romano, Evan Patterson, and Emmanuel J. Candès. Conformalized quantile regression. In *Advances in Neural Information Processing Systems*, volume 32, pages 3538–3548, 2019.
- [30] Filippo Santambrogio. Optimal transport for applied mathematicians. *Birkäuser, NY*, 55(58-63):94, 2015.
- [31] Charles J. Stone. Optimal global rates of convergence for nonparametric regression. *The Annals of Statistics*, 10(4):1040–1053, 1982.
- [32] Benjamin C. Trabling and Michael M. Bell. Understanding error distributions of hurricane intensity forecasts during rapid intensity changes. *American Meteorological Society*, 2020.
- [33] Cédric Villani. *Topics in optimal transportation*, volume 58. American Mathematical Soc., 2021.
- [34] Vladimir Vovk, Alexander Gammernan, and Glenn Shafer. *Algorithmic Learning in a Random World*. Springer, New York, 2005.
- [35] Antoine Wehenkel and Gilles Louppe. Unconstrained monotonic neural networks. *Advances in Neural Information Processing Systems*, 2019.

- [36] David Zhao, Niccolò Dalmaso, Rafael Izbicki, and Ann B. Lee. Diagnostics for conditional density models and bayesian inference algorithms. In Cassio de Campos and Marloes H. Maathuis, editors, *Proceedings of the Thirty-Seventh Conference on Uncertainty in Artificial Intelligence*, volume 161 of *Proceedings of Machine Learning Research*, pages 1830–1840. PMLR, 27–30 Jul 2021. URL <https://proceedings.mlr.press/v161/zhao21b.html>.
- [37] Stephen Zhao, Rob Brekelmans, Alrieza Makhzani, and Roger Baker Grosse. Probabilistic inference in language models via twisted sequential monte carlo. *Proceedings of Machine Learning Research*, 235, 2024.
- [38] Yan Zhou, Fuzhen Wei, Kaiyang Kuang, and Rabea Jamil Mahfoud. Research on a deep ensemble learning model for the ultra-short term probabilistic prediction of wind power. *Electronics*, 13, 2024.

Appendix A: Local diagnostics via PIT-CDF

See Sections 3.1-3.2 for notation and terminology. The local diagnostics framework for conditional density models first occurred in [36].

Local calibration. Given a fixed baseline predictive distribution $\widehat{F}_{Y|X}$, we define the conditional PIT-CDF by

$$G(\alpha | X) := \mathbb{P}\left(\widehat{F}(Y|X) \leq \alpha | x\right), \quad (10)$$

for $\alpha \in [0, 1]$. The base model is *locally calibrated* at a fixed covariate value $x \in \mathcal{X}$ —that is, the predictive PDF $\widehat{f}(y|x) = f(y|x)$ for every $y \in \mathcal{Y}$ —if, and only if, $\widehat{F}(Y|X) | X = x$ is uniformly distributed on $[0, 1]$, or equivalently

$$G(\alpha | x) = \gamma \text{ for every } \alpha \in [0, 1].$$

Diagnostic plots. To visually inspect whether our base model $\widehat{F}_{Y|X}$ is locally calibrated at a given point $x \in \mathcal{X}$, we first evaluate our estimated PIT-CDF regression model \widehat{G} for an IID test sample $\{X_i, Y_i\}_{i=1}^n$, where each X_i is drawn from some distribution over \mathcal{X} , and $Y_i|X_i$ is drawn from the true predictive distribution $F_{Y|X}$.² We then plot $\widehat{G}(\alpha|x)$ versus α , for a grid of α -values in $[0, 1]$. Figure 6 gives an example of how these “diagnostic probability-probability plots” can display failure models like bias, dispersion, skewness, and tailweight of the base model $\widehat{F}_{Y|X}$, relative to the true predictive distribution $F_{Y|X}$ of the test data.

Local discrepancy score. We define a *one-number summary statistic* to assess how well-calibrated the base model \widehat{F} is, for a fixed $x \in \mathcal{X}$, according to our estimated PIT-CDF. More specifically, we compute the *local discrepancy score* (LDS) according to

$$\text{LDS}(x) = \frac{1}{|\Gamma|} \sum_{\alpha \in \Gamma} \left(\widehat{G}(\alpha | x) - \alpha\right)^2, \quad (11)$$

where Γ represents a set of points on an evenly spaced grid over $[0, 1]$. Geometrically, the LDS corresponds to the sum-of-squared deviation between the estimated PIT-CDF curve and the bisector in the local diagnostic plots. Note that when the PIT-CDF is used as a “transport map” to reshape the base model, we can directly relate the error in the reshaped predictive distribution \widetilde{F} at a point (x, y) to the discrepancy between the true transport map G and its parametric approximation at the probability $p := \widehat{F}(y | x) \in [0, 1]$; see Proposition 5.2 for details.

²Calibration and test data typically represent independent samples from the same data-generating process $F_{Y|X}$. Both data sets are assumed to be independent from the data used to learn the base model $\widehat{F}_{Y|X}$.

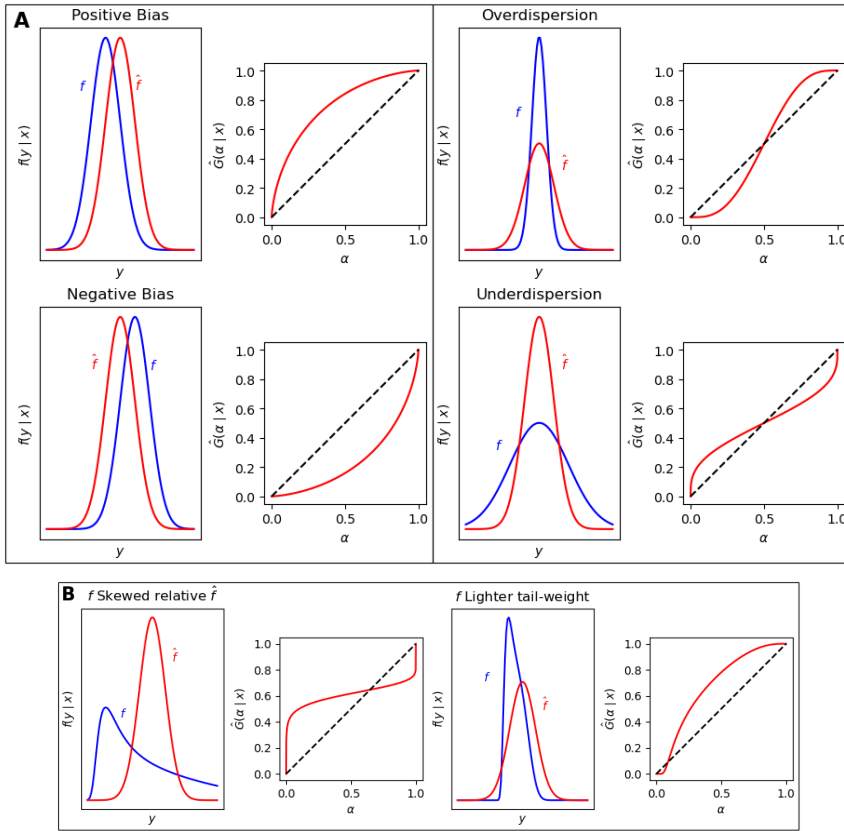


Fig 6. Examples showcasing how different failure modes of the initial density model \hat{f} are diagnosed using probability-probability plots that map $\alpha \rightarrow \hat{G}(\alpha | x)$, where $\hat{G}(\cdot | x)$ is the estimated conditional PIT-CDF. Panel A: To the left, the initial density \hat{f} is shifted toward larger outcome values (“Positive bias”) or toward smaller outcome values (“Negative bias”) relative to the true density f . To the right, the initial density \hat{f} is too wide (“Overdispersion”) or too narrow (“Underdispersion”) relative to the true density f . Panel B: In these examples, \hat{f} and f have the same mean and variance. To the left, the true unknown density f (blue) is skewed to the right; hence a diagnostic plot that signals both positively bias and underdispersion. To the right, the true unknown density f (blue) is also skewed to the right but with lighter tail-weight; hence a diagnostic plot that signals positive bias with slight overdispersion.

Appendix B: CRPS in conditional density estimation (CDE)

In the context of conditional density estimation, the continuous ranked probability score (CRPS) L_{CRPS} measures the accuracy of an estimated conditional density $\tilde{f}(y | x)$ through its predictive cumulative distribution function (CDF) $\tilde{F}(y | x)$ according to

Definition B.1 (CRPS). The continuous ranked probability score is defined by

$$L_{\text{CRPS}}(\tilde{f}; x, y) = \int_{-\infty}^{\infty} (\tilde{F}(t | x) - \mathbb{I}(y \leq t))^2 dt, \quad (12)$$

where $\tilde{F}(t | x) = \int_{-\infty}^t \tilde{f}(s | x) ds$.

Given a validation sample $\mathcal{V} = \{(X_1, Y_1), \dots, (X_m, Y_m)\}$, we estimate the CRPS loss on an evenly spaced grid $[t_1, \dots, t_m]$ according to

$$\widehat{L}_{\text{CRPS}}(\tilde{f}; \mathcal{V}) = \frac{\Delta_t}{m} \sum_{j=1}^m \left(\tilde{F}(t_j | X_i) - \mathbb{I}(Y_i \leq t_j) \right)^2$$

where Δ_t is the grid spacing between $t_j - t_{j-1}$.

Proposition B.2. (Local CRPS) *The conditional expectation of the CRPS loss given $X = x$ for fixed \tilde{f} is the integrated squared error (ISE) of the predictive CDF up to a constant that does not depend on \tilde{F} :*

$$\mathbb{E}[L_{\text{CRPS}}(\tilde{f}; X, Y) | x] = \int_{-\infty}^{\infty} (\tilde{F}(t | x) - F(t | x))^2 dt + K, \quad (13)$$

where $K = \int_{-\infty}^{\infty} \mathbb{E}[(F(t | x) - \mathbb{I}(Y \leq t))^2 | x] dt$.

Proof. The conditional expectation of the CRPS loss given $X = x$ is

$$\mathbb{E}[L_{\text{CRPS}}(\tilde{f}; X, Y) | x] = \mathbb{E}\left[\int_{-\infty}^{\infty} (\tilde{F}(t | x) - F(t | x) + F(t | x) - \mathbb{I}(Y \leq t))^2 dt | x \right]$$

By expanding the square and by changing the order of expectation and integration, we have:

$$\begin{aligned} \mathbb{E}[L_{\text{CRPS}}(\tilde{f}; X, Y) | x] &= \mathbb{E}\left[\int_{-\infty}^{\infty} (\tilde{F}(t | x) - F(t | x))^2 dt | x \right] \\ &\quad + 2 \int_{-\infty}^{\infty} (\tilde{F}(t | x) - F(t | x)) \mathbb{E}[(F(t | x) - \mathbb{I}(Y \leq t)) | x] dt \\ &\quad + \int_{-\infty}^{\infty} \mathbb{E}[(F(t | x) - \mathbb{I}(Y \leq t))^2 | x] dt \end{aligned}$$

Note that:

- The first term represents the squared distance between \tilde{F} and F and is minimized when $\tilde{F}(\cdot | x) = F(\cdot | x)$.
- The second term equals zero

$$\mathbb{E}[F(t | x) - \mathbb{I}(Y \leq t) | x] = F(t | x) - \mathbb{E}[\mathbb{I}(Y \leq t) | x] = F(t | x) - F(t | x) = 0$$

- The third term is a constant that does not depend on \tilde{F} .

The result follows. \square

For the synthetic example in Section 6, we compute the ISE of the reshaped CDF at fixed x via the conditional PIT-CDF and the base model CDF at x :

$$\begin{aligned} \mathcal{E}(x) &:= \int_{-\infty}^{\infty} (\tilde{F}(t | x) - F(t | x))^2 dt \\ &= \int_0^1 \frac{(\tilde{G}(p | x) - G(p | x))^2}{\tilde{f}(u|x)} dp, \end{aligned} \quad (14)$$

where $u = \tilde{F}^{-1}(p|x)$.

Appendix C: Proper loss functions for conditional density estimation

Definition C.1. (Proper loss function) Let $L(\tilde{f}; x, y)$ be a loss function $L : \mathcal{F} \times \mathcal{X} \times \mathcal{Y} \rightarrow \mathbb{R}$ describing the discrepancy between a conditional density estimator \tilde{f} and the true conditional density f of Y given X . The loss $L(\tilde{f}; x, y)$ is proper if and only if

$$f = \arg \min_{\tilde{f} \in \mathcal{F}} \mathbb{E} \left[L(\tilde{f}; x, y) \right].$$

Theorem C.2. The CRPS loss function $L_{\text{CRPS}}(\tilde{f}; x, y)$ is proper.

Proof. The result follows directly from Proposition B.2. \square

Note that the standard formulation of the CRPS (Equation 12) is equivalent to an integrated quantile (or pinball) loss function via

$$\begin{aligned} L_{\text{CRPS}}(\tilde{f}; x, y) &= \int_{-\infty}^{\infty} (\tilde{F}(t | x) - \mathbb{I}(y \leq t))^2 dt \\ &= \int_0^1 2L_{\alpha}(\tilde{F}^{-1}; x, y) d\alpha \end{aligned} \quad (15)$$

where $L_{\alpha}(\tilde{F}^{-1}; x, y) := \left(\tilde{F}^{-1}(\alpha | x) - y \right) \left(\mathbb{I}(y \leq \tilde{F}^{-1}(\alpha | x)) - \alpha \right)$ is the standard pinball loss of the quantile forecast $\tilde{F}^{-1}(\alpha|x)$ evaluated at (x, y) . This result can be found in [26, 15] with a general proof in Appendix A of [12].

Depending on the application, one might choose threshold-weighted or quantile-weighted versions of the CRPS [15]

$$L_{\text{CRPS}}(\tilde{f}; x, y) = \int_{-\infty}^{\infty} (\tilde{F}(t | x) - \mathbb{I}(y \leq t))^2 u(t) dt$$

and

$$L_{\text{CRPS}}(\tilde{f}; x, y) = \int_0^1 2L_{\alpha}(\tilde{F}^{-1}; x, y) v(\alpha) d\alpha,$$

with non-negative weight functions $u(\cdot)$ and $v(\cdot)$ on the real line \mathbb{R} and unit interval $[0, 1]$, respectively.

Finally, Theorem 1 in [36] shows that a uniform standard (marginal) PIT score does not necessarily imply that the conditional density is well estimated, whereas Theorem 2 shows that the *conditional* PIT-CDF uniquely characterizes the CDE.

Appendix D: Proofs for Section 3

Proof of Lemma 3.1. Since $\widehat{F}(\cdot | x)$ is strictly increasing, the events $\{Y \leq y\}$ and $\{\widehat{F}(Y | x) \leq \widehat{F}(y | x)\}$ coincide. Thus

$$F(y | x) = \mathbb{P}(Y \leq y | X = x) = \mathbb{P}(\widehat{F}(Y | x) \leq \widehat{F}(y | x) | X = x) = G(\widehat{F}(y | x) | x).$$

□

Proof of Corollary 3.3. According to Lemma 3.1, the reshaped predictive CDF is $\widetilde{F}(t | x) = \widehat{G}(\widehat{F}(t | x) | x)$ and the true predictive CDF can be expressed as $F(t | x) = G(\widehat{F}(t | x) | x)$. Thus,

$$|\widetilde{F}(t | x) - F(t | x)| = |\widehat{G}(\widehat{F}(t | x) | x) - G(\widehat{F}(t | x) | x)| = |\widehat{G}(\widehat{F}(t | x) | x) - G(\widehat{F}(t | x) | x)|$$

□

Appendix E: Proofs for Section 5

Proof of Proposition 5.2. By Lemma 3.1,

$$F(y | x) = G(p | x), \quad \widetilde{F}(y | x) = G_{\widehat{\beta}}(p | x),$$

so that the pointwise calibration error is

$$|F(y | x) - \widetilde{F}(y | x)| = |G(p | x) - G_{\widehat{\beta}}(p | x)|.$$

The conclusion follows from the triangle inequality. □

Appendix F: Optimal transport

Here we briefly review Monge's continuous formulation of the OT distance; see [33] for a more complete and mathematical description of OT.

Consider two distributions F_0 and F defined over respective domains $\Omega_0, \Omega \subseteq \mathbb{R}^d$. Monge's OT problem is to find a function $T : \Omega_0 \rightarrow \Omega$ that pushes F_0 onto F and minimizes the distance

$$d(F_0, F) = \inf_T \int \|x - T(x)\|^p dF_0(x)$$

subject to $T(X) \sim F$, where $p \geq 1$ and $X \sim F_0$. Such a minimizer T^* exists if F_0 and F both have densities. The minimizer T^* is called the *optimal transport map*. The map

$$T_s(x) = (1 - s)x + sT^*(x), \tag{16}$$

for $s \in [0, 1]$ gives the path of a particle of mass at x . The distribution of $T_s(X)$ is also the geodesic (that is, the shortest path according to the metric d) connecting F_0 to F ; see [24] for a technical definition.

If $\Omega = \Omega_0 = \mathbb{R}$ and both F and F_0 are absolutely continuous, with continuous densities which do not vanish, the optimal transport is given by

$$T(x) = F^{-1}(F_0(x)).$$

See [30] for a detailed survey.

Appendix G: The diagnostic transport map corresponds to an optimal transport

The PIT-based representation from Lemma 3.1 admits a natural interpretation in terms of one-dimensional optimal transport (OT). In this view, the PIT-CDF $G(\cdot | x)$ encodes a transport map between the initial predictive distribution $\widehat{F}(\cdot | x)$ and the true distribution $F(\cdot | x)$ in probability space. An estimated diagnostic transport map then induces a full transportation map in outcome space, providing a continuous path from the original to the calibrated predictive distribution.

G.1. One-dimensional OT between $\widehat{F}(\cdot | x)$ and $F(\cdot | x)$

Fix $x \in \mathcal{X}$ and consider the two conditional distributions $\widehat{F}(\cdot | x)$ and $F(\cdot | x)$ of Y given $X = x$. Let μ_x and ν_x denote the corresponding probability measures on \mathbb{R} . For a cost function $c(y, y') = |y - y'|^p$ with $p \geq 1$, the one-dimensional Monge OT problem seeks a measurable map $T_x : \mathbb{R} \rightarrow \mathbb{R}$ that pushes μ_x forward to ν_x and minimizes $\int |y - T_x(y)|^p d\mu_x(y)$. In one dimension, when both distributions are continuous and strictly increasing, the unique optimal map is the monotone rearrangement given by

$$T_x(y) := F^{-1}(\widehat{F}(y | x) | x).$$

G.2. Expressing the OT map in terms of the PIT-CDF

The OT map T_x can be expressed purely in terms of the base model CDF \widehat{F} and the PIT-CDF G . Recall that for fixed x ,

$$G(\alpha | x) = \mathbb{P}(\widehat{F}(Y | x) \leq \alpha | X = x).$$

In Section 3.3, we introduced Proposition 3.4, which we will now formally prove.

Proof. Fix x and define $u := \widehat{F}(y | x) \in [0, 1]$. By the PIT identity (Lemma 3.1), we may write

$$G(\alpha | x) = F(\widehat{F}^{-1}(\alpha | x) | x), \quad \alpha \in [0, 1].$$

For any $\tau \in [0, 1]$, the equation $G(\alpha | x) = \tau$ is equivalent to

$$F(\widehat{F}^{-1}(\alpha | x) | x) = \tau.$$

Thus, if $\alpha = G^{-1}(\tau | x)$, then

$$F^{-1}(\tau | x) = \widehat{F}^{-1}(\alpha | x) = \widehat{F}^{-1}(G^{-1}(\tau | x) | x).$$

Setting $\tau = u = \widehat{F}(y | x)$ yields

$$T_x(y) = F^{-1}(\widehat{F}(y | x) | x) = \widehat{F}^{-1}\left(G^{-1}(\widehat{F}(y | x) | x) \mid x\right),$$

as claimed. \square

Proposition 3.4 shows that the OT map is fully determined by the base model $\widehat{F}(\cdot | x)$ and the PIT-CDF $G(\cdot | x)$. In practice, we replace G by an estimate \widehat{G} obtained via parametric or nonparametric models and invert both \widehat{G} and \widehat{F} numerically.

Appendix H: Derivation of bounds

H.1. Bounds under Lipschitz regularity and parametric rates

To control the estimation term in Proposition 5.2, we assume that the PIT-CDF is locally Lipschitz in the parameter vector β .

Assumption 1 (Local Lipschitz continuity in β). *For each $(x, u) \in \mathcal{X} \times [0, 1]$ there exists a constant $C(x, u) < \infty$ such that*

$$|G_{\beta_1}(u | x) - G_{\beta_2}(u | x)| \leq C(x, u) \|\beta_1 - \beta_2\| \quad \text{for all } \beta_1, \beta_2 \in \mathcal{B}.$$

This assumption is natural for smoothly parameterized parametric families and neural networks whose outputs vary smoothly with respect to their weights.

Corollary H.1 (Pointwise bias–variance bound). *Under Assumption 1, for every $x \in \mathcal{X}$, $c \in \mathcal{Y}$, and $u = \widehat{F}(c | x)$,*

$$|F(c | x) - \widetilde{F}(c | x)| \leq \underbrace{|G(u | x) - G^*(u | x)|}_{\text{PIT misspecification}} + \underbrace{C(x, u) \|\widehat{\beta} - \beta^*\|}_{\text{estimation error}}.$$

We next assume a standard parametric estimation rate for $\widehat{\beta}$.

Assumption 2 (Parametric convergence rate). *There exists a constant $C < \infty$ such that*

$$\mathbb{E}[\|\widehat{\beta} - \beta^*\|^2] \leq \frac{C}{N}.$$

Assumption 2 is the usual $1/N$ mean-square rate for regular estimators in \mathbb{R}^q (e.g. maximum likelihood or smooth M-estimators under regularity conditions). To obtain an integrated error bound, fix $x \in \mathcal{X}$ and consider

$$\mathcal{E}(x) := \int_{\mathcal{Y}} (F(c | x) - \widetilde{F}(c | x))^2 w(dc),$$

for an arbitrary weighting measure w on \mathcal{Y} .

Theorem H.2 (Bound on integrated error). *Under Assumptions 1 and 2, we have*

$$\mathbb{E}[\mathcal{E}(x)] \leq 2 \int_{\mathbf{y}} (G(u_c | x) - G^*(u_c | x))^2 w(dc) + \frac{2\tilde{C}(x)}{N},$$

where $u_c := \widehat{F}(c | x)$ and

$$\tilde{C}(x) := C \int_{\mathbf{y}} C(x, u_c)^2 w(dc).$$

The first term is the irreducible PIT-model misspecification, while the second term vanishes at rate $1/N$.

Proof. By Proposition 5.2 and Assumption 1,

$$|F(c | x) - \tilde{F}(c | x)| \leq |G(u_c | x) - G^*(u_c | x)| + C(x, u_c) \|\widehat{\beta} - \beta^*\|.$$

Squaring both sides and using $(a + b)^2 \leq 2a^2 + 2b^2$ yields

$$(F(c | x) - \tilde{F}(c | x))^2 \leq 2(G(u_c | x) - G^*(u_c | x))^2 + 2C(x, u_c)^2 \|\widehat{\beta} - \beta^*\|^2.$$

Integrating over c with respect to w gives

$$\mathcal{E}(x) \leq 2 \int_{\mathbf{y}} (G(u_c | x) - G^*(u_c | x))^2 w(dc) + 2\|\widehat{\beta} - \beta^*\|^2 \int_{\mathbf{y}} C(x, u_c)^2 w(dc).$$

Taking expectations and applying Assumption 2 completes the proof. \square

H.2. Nonparametric PIT estimation

In the fully nonparametric version, we estimate $G(\alpha | x)$ from the calibration sample without imposing a parametric shape in α . Let \mathcal{H} be a function class of conditional CDFs,

$$\mathcal{H} \subset \left\{ H : [0, 1] \times \mathcal{X} \rightarrow [0, 1] \text{ such that } \alpha \mapsto H(\alpha | x) \text{ is a CDF for each } x \right\}.$$

Let $\widehat{H}(\alpha | x) \in \mathcal{H}$ be any estimator of $G(\alpha | x)$ computed from $\{(X_i, Z_i)\}_{i=1}^N$, and define

$$\tilde{F}^{\text{np}}(y | x) := \widehat{H}(\widehat{F}(y | x) | x).$$

Define the integrated calibration error at x as

$$\mathcal{E}^{\text{np}}(x) := \int_{\mathbf{y}} (F(c | x) - \tilde{F}^{\text{np}}(c | x))^2 w(dc).$$

We make the following assumption:

Assumption 3 (Integrated nonparametric PIT error rate at fixed x). *Fix $x \in \mathcal{X}$. Assume $G(\cdot | x) \in \mathcal{H}$. There exist constants $s > 0$ and $C_{\text{np}}(x) < \infty$ such that*

$$\mathbb{E}[\mathcal{E}^{\text{np}}(x)] \leq C_{\text{np}}(x) N^{-2s/(2s+d)}.$$

This assumption can be justified by the fact that a standard way to estimate $F(\cdot | x)$ is to treat

$$F(c | x) = \mathbb{E}[\mathbb{I}\{Y \leq c\} | X = x]$$

as a nonparametric regression function in x for each threshold c . Under s -smoothness in x , pointwise mean-square rates at a fixed x match the usual nonparametric regression rate $N^{-2s/(2s+d)}$, and integrating over c does not change the exponent. This perspective for conditional CDF estimation appears, for example in [17, 18], and the base model minimax regression rate goes back to [31].

Appendix I: Additional results for the synthetic example

Lemma I.1. *When $\widehat{F}(y | \mathbf{X}) \stackrel{d}{=} N(0, 1)$ and $F(y | \mathbf{X})$ is known, the true conditional PIT-CDF at α is*

$$G(\alpha | \mathbf{X}) = F(\Phi^{-1}(\alpha) | \mathbf{X})$$

Proof. Say that $U = \Phi(Y)$. The conditional PIT-CDF is defined as $\mathbb{P}(U \leq u | \mathbf{X})$.

$$\mathbb{P}(U \leq u | \mathbf{X}) = \mathbb{P}(\Phi(Y) \leq u | \mathbf{X}) = \mathbb{P}(Y \leq \Phi^{-1}(u) | \mathbf{X})$$

By definition, this is the CDF of the SAS distribution evaluated at $\Phi^{-1}(u)$. Therefore,

$$G(\alpha | \mathbf{X}) = F(\Phi^{-1}(\alpha) | \mathbf{X})$$

□

The PIT-CDF was approximated parametrically by minimizing the negative log-likelihood of a, b , an approximation to the best-in-family $a^*(\mathbf{X}), b^*(\mathbf{X})$ for the Kumaraswamy distribution. Given this set-up, the following holds:

Proposition I.2 (Parametric irreducible error). *The irreducible error in the parametric conditional PIT-CDF approximation at α is*

$$|G(\alpha | \mathbf{X}) - G^*(\alpha | \mathbf{X})| = |F_{Y|\mathbf{X}}(\Phi^{-1}(\alpha) | \mathbf{X}) - 1 + (1 - \alpha^{a^*(\mathbf{X})})^{b^*(\mathbf{X})}|$$

Proof. By Lemma I.1, the true conditional PIT-CDF for this example is $F(\Phi^{-1}(\alpha) | \mathbf{X})$. The proposition follows from the fact that the CDF of the Kumaraswamy distribution is

$$G(\alpha) = 1 - (1 - \alpha^a)^b.$$

□

The convergence rate of the maximum likelihood estimator for the Kumaraswamy to the best-in-family parameter is as follows:

Lemma I.3 (Convergence of the MLE to the best-in-family). *The maximum likelihood estimator for the Kumaraswamy distribution converges at a rate of $n^{-1/2}$ to the Kullback-Leibler best-in-family parameter θ^* .*

Proof. The Kumarswamy log-density is smooth, twice differentiable, and identifiable. Assume that θ^* lies in the boundary $(0, 1)$.

The maximum likelihood estimator $\widehat{\theta}_n$ maximizes the log-likelihood

$$l_n(\theta) = \frac{1}{n} \sum_{i=1}^n \log(f(X_i; \theta))$$

The best-in-family parameter θ^* can be defined as

$$\theta^* = \arg \max_{\theta} \mathbb{E}_{P_0} [\log(f(X_i; \theta))]$$

where P_0 is the true distribution.

By the uniform law of large numbers

$$\sup_{\theta \in \Theta} [l_n(\theta) - \mathbb{E}_{P_0} [\log(f(X_i; \theta))]] \xrightarrow{P} 0$$

If we assume θ^* to be a unique maximizer and that Θ is compact, then by the continuous mapping theorem, $\widehat{\theta}_n \xrightarrow{P} \theta^*$.

By definition

$$0 = \nabla l_n(\widehat{\theta}_n)$$

We can Taylor expand around θ^*

$$0 = \nabla l_n(\theta^*) + \nabla^2 l_n(\widetilde{\theta}_n)(\widehat{\theta}_n - \theta^*)$$

where $\widetilde{\theta}_n \in (\widehat{\theta}_n, \theta^*)$.

By the central limit theorem,

$$\sqrt{n}(\nabla l_n(\theta^*)) = \frac{1}{n} \sum_{i=1}^n \nabla \log(f(X_i; \theta^*)) \xrightarrow{d} N(0, J)$$

where $J = \text{Var}_{P_0}[\nabla \log(f(X_i; \theta^*))]$.

By the law of large numbers

$$\nabla^2 l_n(\widetilde{\theta}_n) \xrightarrow{P} H = \mathbb{E}_{P_0} [\nabla^2 \log(f(X_i; \theta^*))]$$

where H is the negative definite Hessian.

Then by the Taylor expansion we get

$$\sqrt{n}(\widehat{\theta}_n - \theta^*) = -H^{-1} \sqrt{n} \nabla l_n(\theta^*) + o_p(1)$$

Therefore,

$$\sqrt{n}(\widehat{\theta}_n - \theta^*) \xrightarrow{d} N(0, H^{-1} J H^{-1})$$

Thus, $|\widehat{\theta}_n - \theta^*| = O_p\left(\frac{1}{\sqrt{n}}\right)$

□

Appendix J: Details on the TC data

For calibration, we use the “NHC forecast error” [6], which is defined as the residual of the NHC’s operational intensity estimate relative to the best-track intensity data provided by NOAA’s Hurricane Database 2 (HURDAT2) [7]. The 2022 SHIPS predictor file [5] contains approximately 90 environmental predictors for the forecasting of hurricane intensity. The input sequence $\mathbf{S}_{\leq t}$ used to forecast the TC intensity error distribution $f(\epsilon_{t+24} \mid \mathbf{S}_{\leq t})$ at a 24-hour lead time include the TC intensity (in knots) and a subset of the following 13 SHIPS predictors at $t - 12$, $t - 6$ and t hours:

- Maximum surface wind (knots)
- Shear magnitude (knots * 10) from 850-200 hPa
- Shear magnitude (knots * 10) from 850-200 hPa at 200-800 km
- Shear magnitude (knots * 10) with vortex removed and averaged from 0-500 km relative to the 850 hPa vortex center
- Relative humidity (%) from 850-700 hPa at 200-800 km
- Relative humidity (%) from 700-500 hPa at 200-800 km
- Relative humidity (%) from 500-300 hPa at 200-800 km
- Maximum potential intensity from the Kerry Emanuel equation (knots)
- Zonal wind (knots * 10) at 200 hPa for 200-800 km
- Intensity change (knots) from $t = 0$
- Distance to nearest major land mass (km)
- Latitude (degrees North * 10)
- Longitude (degrees West * 10)

SHIPS predictors were matched to intensity errors from the NHC’s operational forecast [6] through dates, times, latitudes, and longitudes. If a particular SHIPS predictor was null (represented by a 9999 in the file) for $t - 12$, $t - 6$, and t or if the NHC failed to report an intensity error at $t + 24$, that storm sequence was removed entirely from the data set. If a subset of the data was missing, missing values were interpolated using the previous time point’s measurement. Storm sequences were only considered once they were classified as a tropical cyclone (intensity > 34 knots); tropical depressions were not considered.

Appendix K: Additional results for the TC application

K.1. Convergence rates of diagnostic transport maps

From Table 2 it is evident that the parametric map outperforms the nonparametric map in terms of CRPS and RMSE forecast errors across different storm categories. This result is a consequence of the limited sample size N of \mathcal{T}_{cal} ; see Section 5 for a theoretical discussion (note that the ISE of the predictive CDF is the same as the local CRPS loss up to a constant; Proposition B.2). In Figure 7, we illustrate the difference in the average CRPS (Equation 12) for parametric versus nonparametric diagnostic transport maps empirically by downsampling the TC calibration data in Table 1, while keeping the test data the same.

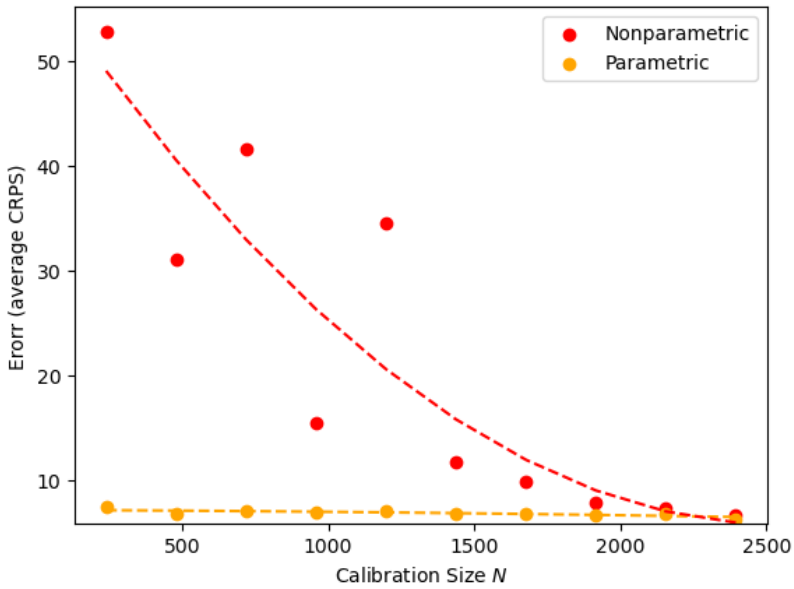


Fig 7. Convergence rates of diagnostic transport maps for TC application. *The markers show the average CRPS as a function of the calibration size N for nonparametric (red) versus parametric (orange) maps. We randomly downsampled the calibration set, while keeping the test set the same as in Table 1. The results indicate that the parametric error quickly converges to the (non-zero) best-in-family error and remains approximately constant for most values of N . The nonparametric error eventually converges to zero but at much larger sample sizes N . Note that we only have a total of $N = 2395$ calibration sequences between Years 2000-2015 for the North Atlantic basin.*

K.2. Diagnostic insights for TC application

Diagnostic transport maps improve the most upon NHC error distributions for intense storms and rapid intensity change events. In Section 7.3, we showed visualizations for an ill-calibrated error distribution for an intense storm. Figure 8 shows similar visuals for another input sequence with a poor NHC error estimate: Point C in the diagnostic plot of Panel I (left) here corresponds to a sequence when Hurricane Maria (2017) underwent rapid weakening. Diagnostic transport maps are again able to shift the error distribution at $t + 24$ hours towards the true intensity error of 0.

